Exploration Geophysics

ISSN: 0812-3985 (Print) 1834-7533 (Online) Journal homepage: https://www.tandfonline.com/loi/texg20

DC modelling in 2.5-D anisotropic media with singularity removal

Tao Song, Yun Liu & Yun Wang

To cite this article: Tao Song, Yun Liu & Yun Wang (2019) DC modelling in 2.5-D anisotropic media with singularity removal, Exploration Geophysics, 50:3, 221-232, DOI: 10.1080/08123985.2019.1590119

To link to this article: https://doi.org/10.1080/08123985.2019.1590119

Published online: 22 Apr 2019.

EXPLORATION GEOPHYSICS
2019, VOL. 50, NO. 3, 221–232
https://doi.org/10.1080/08123985.2019.1590119

Taylor & Francis
Taylor & Francis Group

DC modelling in 2.5-D anisotropic media with singularity removal

Tao Song [a], Yun Liu[a] and Yun Wang[b]

[a]State Key Laboratory of Ore Deposit Geochemistry, Institute of Geochemistry Chinese Academy of Sciences, Gui Yang, China; [b]School of Geophysics and Information Technology, China University of Geosciences, Beijing, China

ABSTRACT

We present a 2.5-dimensional (2.5-D) finite element algorithm for direct current (DC) resistivity modelling in anisotropic media with singularity removal. First, we provide the weak form of the integral equation for the boundary value problem and simplify the Euler angles while calculating the primary potential so that the Fourier transform of the background potential with the dip angle can be avoided because it is mathematically difficult. A two-layered model is then simulated when the first covering is anisotropic. The relative error between this numerical solution and the analytical solution is $< 1\%$. We then model a number of more complicated scenarios, using the algorithm developed in this paper. We test the model response to a small body at depth whose resistivity is isotropic, and then test whether the longitudinal or transverse resistivities affect the final results more. Based on this analysis, we found that longitudinal resistivity has more of an effect on the apparent resistivity than transverse resistivity in collinear arrays, such as pole–pole, dipole–dipole and Wenner arrays. Finally, through calculation of the current density and anomalous current density of several arrays, we conclude that the causes of different responses of longitudinal and transverse resistivity by each array is the distribution of current density in the subsurface. We also show that the sensitivity of each array type to variations in longitudinal and transverse resistivity can be understood when looked at from the perspective of current density.

ARTICLE HISTORY
Received 22 November 2017
Accepted 25 February 2019

KEYWORDS
Singularity removal; anisotropic media; current density; longitudinal resistivity; transverse resistivity

Introduction

Modelling and inversion techniques for data collected using direct current (DC) resistivity based on isotropic media are well developed. Unfortunately, the electric conductivity of the Earth's subsurface is often anisotropic; research and simulation based on anisotropic media is becoming a popular topic. Asten (1974) obtained an analytical solution for a current point source in a homogeneous anisotropic half-space in which one of the principal axes is parallel to the ground surface. Lindell et al. (1993) used an image source method to compute the electrical potential in an azimuthally anisotropic half-space caused by current point current, but did not provide an analytical solution for the arbitrarily anisotropic half-space. Li and Uren (1997a, 1997b) also adopted the image source method to deduce and compute the field potential in three-dimensional (3-D) arbitrarily anisotropic half-space; they also deduced and analysed the potential features of 3-D anisotropic half-space with two horizontal layer and two vertical boundary planes, respectively. All this research has laid the foundation for further study of the effects of anisotropy.

Some numerical methods have been adopted in research regarding DC anisotropic media modelling. Li and Uren (1997c) presented an approach to compute the DC potential in an arbitrarily anisotropic half-space with an embedded 3-D perfect conductor by solving the integral equation that arises from the current point source. Through their simulation, they concluded that neglecting the anisotropy effect on the potential could lead to serious misinterpretations of field data and that forward modelling would also aid interpretations. Yin and Weidelt (1999) provided the analytical solution for a DC, one-dimensional (1-D) layered earth with arbitrarily anisotropic media and investigated the 1-D inversion. They concluded that the non-uniqueness in the geoelectrical inversion for an anisotropic model is inherent, even with sufficient and accurate data (Yin 2000). This consequence supports the difficulty associated with the inversion of anisotropic media. Li and Spitzer (2005) present a 3-D finite element (FE) scheme for DC resistivity modelling in anisotropic media using parallelepiped-shaped elements. Later, Zhou, Greenhalgh, and Greenhalgh (2009) presented a new numerical scheme called Gaussian quadrature grids (GQG) for 2.5-/3-D DC resistivity modelling in anisotropic media that makes it easier to deal with complex topography than using traditional methods. The unstructured grid and adaptive FE method (Ren and Tang 2010, 2014)

CONTACT Tao Song songtao@mail.gyig.ac.cn State Key Laboratory of Ore Deposit Geochemistry, Institute of Geochemistry Chinese Academy of Sciences, Gui Yang 550081, China

are introduced into the modelling of 3-D DC resistivity, which leads to greater accuracy and the ability to model complex formation and topography. Wang, Wu, and Spitzer (2013) proposed an unstructured FE method to DC resistivity modelling in arbitrary anisotropic media and achieved good accuracy.

Normally, the speed of 3-D forward modelling is relatively slow, and inversion research based on the 3-D anisotropy forward problem is rare, because there are too many parameters that need to be inverted, which makes the inversion difficult to converge. Therefore, research on the modelling technique of 2.5-D anisotropic media has become a bridge to explore the anisotropic inversion.

In previous studies, much of the DC work on resistivity forward and inversion for 2.5-D anisotropic media has been based on the total potential approach (Greenhalgh, Wiese, and Marescot 2010; Wiese et al. 2015; Zhou, Greenhalgh, and Greenhalgh 2009), which may lead to relatively large errors due to inadequate representation of the source on a discrete grid (Zhao and Yedlin 1996); using the singularity removal technique would largely increase the accuracy of the numerical results (Li and Spitzer 2002; Lowry, Allen, and Shive 1989; Penz et al. 2013; Ren and Tang 2014; Wu et al. 2003; Zhao and Yedlin 1996). However, for the 2.5-D problem, there is an obstacle in that Fourier transform of primary potential with a dip angle in anisotropic half-space is difficult to calculate. In this paper, we simplify the 2.5-D anisotropic modelling with singularity removal by setting the Euler angles to zero in calculating the Fourier transform. Our results show that the accuracy is sufficiently high when this simplification is used.

Through simulations, we found that varying longitudinal resistivity had more effect on the recorded resistivity response than varying the transverse resistivity when data were collected using the pole–pole, dipole–dipole and Wenner arrays. Li and Uren (1997c) and Li and Spitzer (2005) have analysed the influence of anisotropic parameters from the perspective of potential. In this paper, we calculate the current densities that are generated by three commonly used arrays and analyse their ability to explore longitudinal resistivity and transverse resistivity.

2.5-D forward modelling

Basic equations

In anisotropic media, the resistivity tensor can be written as $\boldsymbol{\rho} = \mathbf{D}\boldsymbol{\rho}_0\mathbf{D}^{\mathbf{T}}$ (Yin 2000) where $\boldsymbol{\rho}_0 = \mathrm{diag}(\rho_x, \rho_y, \rho_z)$, ρ_x, ρ_y and ρ_z represent the resistivity of the three principal axes, and

$$\mathbf{D} = \begin{pmatrix} \cos\gamma\cos\beta & -\sin\gamma\cos\beta & \sin\beta \\ \sin\gamma\cos\alpha & \cos\gamma\cos\alpha & -\cos\beta\sin\alpha \\ +\cos\gamma\sin\beta\sin\alpha & -\sin\gamma\sin\beta\sin\alpha & \\ \sin\gamma\sin\alpha & \cos\gamma\sin\alpha & \cos\beta\cos\alpha \\ -\cos\gamma\sin\beta\cos\alpha & +\sin\gamma\sin\beta\cos\alpha & \end{pmatrix}$$

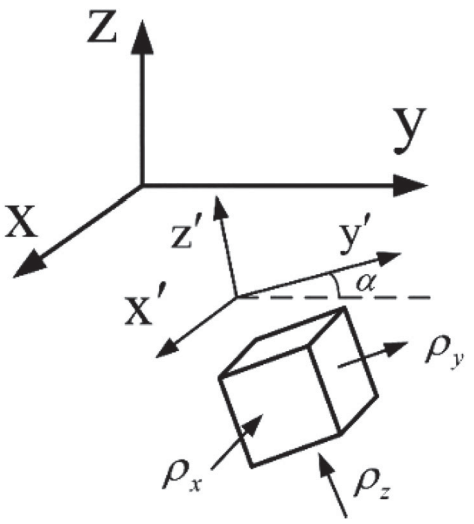

Figure 1. Coordinate system and 2-D anisotropic media.

is a rotation matrix where α, β and γ are three Euler angles. If the resistivity attribute in the x-direction is constant, and if $\rho_0 = diag(\rho_x, \rho_y, \rho_z) = diag(\rho_y, \rho_y, \rho_z)$, then the rotation matrix $\mathbf{D}$ simplifies to $\mathbf{D} = \begin{bmatrix} 1 & 0 & 0 \\ 0 & \cos\alpha & \sin\alpha \\ 0 & -\sin\alpha & \cos\alpha \end{bmatrix}$. The coordinate system and Euler angle α are shown in Figure 1.

The potential that is generated by the point current source satisfies the 2-D differential equation, as shown in Equation (1):

$$\nabla \bullet (\tau \nabla U) - k^2\sigma_y U = -I\delta(A) \tag{1}$$

where ∇ is the 2-D Hamiltonian operator, k is the wavenumber (Dey and Morrison 1979), A indicates the current point source, $\sigma_y = 1/\rho_y$ is the conductivity and τ is the conductive tensor shown in Equation (2).

$$\begin{aligned} \tau &= \begin{bmatrix} \tau_{11} & \tau_{12} \\ \tau_{21} & \tau_{22} \end{bmatrix} \\ &= \begin{bmatrix} \sigma_y\cos^2\alpha + \sigma_z\sin^2\alpha & \frac{1}{2}(\sigma_y - \sigma_z)\sin 2\alpha \\ \frac{1}{2}(\sigma_y - \sigma_z)\sin 2\alpha & \sigma_y\sin^2\alpha + \sigma_z\cos^2\alpha \end{bmatrix} \end{aligned} \tag{2}$$

According to Xu (1994) and Zhou, Greenhalgh, and Greenhalgh (2009), the weak form of the integral equation for the total potential boundary value problem is written as Equation (3):

$$\begin{cases} F(U) = \int_\Omega [\frac{1}{2}\nabla U \cdot (\boldsymbol{\tau}\nabla U) + \frac{1}{2}k^2\sigma_y U^2 - I\delta(A)U]d\Omega \\ + \int_{\Gamma_\infty} k\sigma_y\beta U^2 d\Gamma \\ \delta F(U) = 0 \\ \beta = \dfrac{\mathrm{K}_1(k\sqrt{y^2+\lambda z^2})}{\mathrm{K}_0(k\sqrt{y^2+\lambda z^2})}\dfrac{y\cos\theta + z\sin\theta}{\sqrt{y^2+\lambda z^2}} \end{cases} \tag{3}$$

Where Ω denotes the model area, and Γ_∞ denotes the model boundary except for the surface boundary, K_0 and K_1 are the modified Bessel function of zero order

and first order, respectively (Dey and Morrison 1979; Xu 1994), θ is the angle between the outward unit normal and the boundary (Zhao and Yedlin 1996).

To improve the accuracy of simulation, Lowry, Allen, and Shive (1989) employed a method for removing the source singularity by splitting the potential into the primary potential u_0 and secondary potential u, while u_0 is caused by the current source in a uniform half-space and u is caused by the anomalous conductivity, and the total potential can be stated as:

$$v = u_0 + u \tag{4}$$

Also, the conductivity can be stated as:

$$\sigma = \sigma_0 + \sigma' \tag{5}$$

The primary potential u_0 can be calculated because it has the analytic solution (Zhao and Yedlin 1996), so most of the error is in u; generally u is much smaller than u_0. So, if we calculate the secondary potential u, the result would be more accurate.

Similarly, for the 2-D problem, the weak form of the integral equation with singularity removal is written as:

$$\begin{cases} F(U) = \int_\Omega \left[\frac{1}{2}\nabla U \cdot (\boldsymbol{\tau}\nabla U) + \frac{1}{2}k^2\sigma_y U^2 \right. \\ \left. +\nabla U \cdot (\boldsymbol{\tau}'\nabla U_0) + k^2\sigma_y' U U_0 \right] d\Omega \\ + \int_{\Gamma_\infty} \frac{1}{2} k\sigma_y \beta U^2 d\Gamma + \int_{\Gamma_\infty} k\sigma'_y \beta U U_0 d\Gamma \\ \delta F(U) = 0 \end{cases} \tag{6}$$

where $\sigma_y = \sigma_{y0} + \sigma_y'$, $\boldsymbol{\tau} = \boldsymbol{\tau}_0 + \boldsymbol{\tau}'$, and σ_{y0} and $\boldsymbol{\tau}_0$ are the conductivity and conductivity tensors of background, respectively. σ_y' and $\boldsymbol{\tau}'$ are the anomalous conductivity and anomalous conductivity tensors, respectively.

Comparing Equation (3) and Equation (6), the two expressions are very similar although the current term ($I\delta(A)$) is not included in Equation (6), which eliminates the singularity at the source and improves simulation accuracy.

FE approach

The total area is subdivided into a number of elements with constant resistivity. In Figure 2, the area highlighted by red lines denotes the computation area of interest, and the dashed black lines denote the coarse area. Generally, the distance between nodes in the computation area is fixed (for example, d), so the grid is the same. In the coarse area, the width of the node is calculated by $C_i \cdot d$, where C_i is the coefficient. The larger the distance from the computation area to the node, the greater the coefficient; values are highest at the boundary far from the main computation area.

Each box in the quadrilateral mesh is then divided into four triangles. The final grid is shown in Figure 3, and one triangular element is shown in Figure 4.

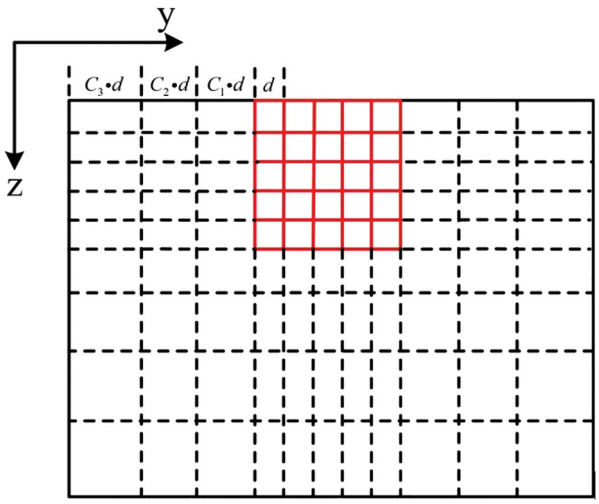

Figure 2. Global region subdivision with coarse area.

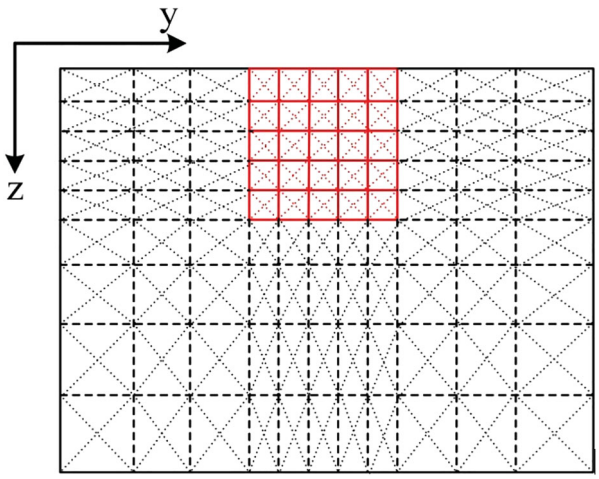

Figure 3. Regional grid segmentation.

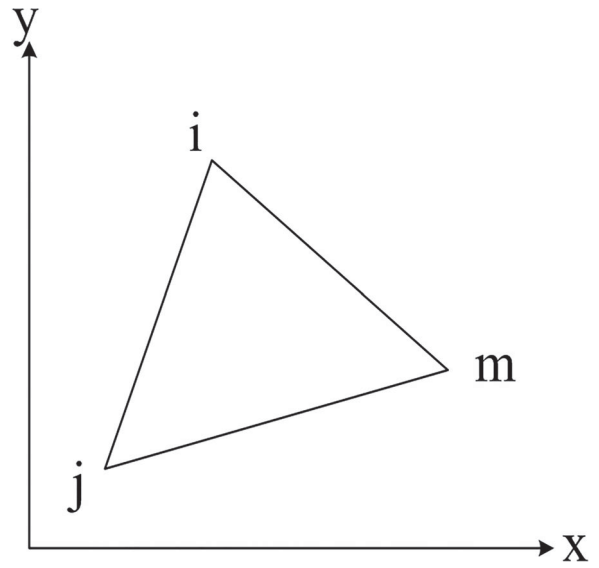

Figure 4. Triangle element.

The potentials are approximated in each element by linear representations, as shown in Equation (7).

$$u = N_i u_i + N_j u_j + N_m u_m = \mathbf{N^T u} = \mathbf{u^T N} \tag{7}$$

where $\mathbf{N^T} = (N_i, N_j, N_m)$ is the shape function, and $\mathbf{u^T} = (u_i, u_j, u_m)$ is the potential at the three triangle vertices.

The integrals in Equation (6) are discretised in the region and expressed as a linear combination of all elements, as shown in Equation (8):

$$\begin{aligned} F(U) = &\sum_{\Omega}\int_e \left[\frac{1}{2}(\nabla U)\cdot(\boldsymbol{\tau}\nabla U)\right]d\Omega \\ &+ \sum_{\Omega}\int_e \left[\frac{1}{2}k^2\sigma_y U^2\right]d\Omega + \sum_{\Omega}\int_e \frac{1}{2}[k\sigma_y\beta U^2]d\Gamma \\ &+ \sum_{\Omega}\int_e [(\nabla U)\cdot(\boldsymbol{\tau}'\nabla U_0)]d\Omega \\ &+ \sum_{\Omega}\int_e [k^2\sigma'_y U U_0]d\Omega \\ &+ \sum_{\Omega}\int_e [k\sigma'_y\beta U U_0]d\Gamma \end{aligned} \tag{8}$$

The integrals in Equation (8) are denoted in turn as integrals 1, 2, 3, 4, 5 and 6. It is apparent that integral 1 is similar to integral 4, and the same is true for integrals 2 and 5, as well as integrals 3 and 6.

Since ∇ is a vector, it can be written as $\nabla^{\mathbf{T}} = (\frac{\partial}{\partial x}, \frac{\partial}{\partial y})$. The main part of integral 1 in Equation (8) can be written as Equation (9).

$$\begin{aligned} (\nabla U)^{\mathbf{T}}\cdot(\boldsymbol{\tau}\nabla U) &= (\nabla \mathbf{N^T u}_e)^{\mathbf{T}}\cdot(\boldsymbol{\tau}\nabla \mathbf{N^T u}_e) \\ &= \mathbf{u^T}(\mathbf{N}\nabla^{\mathbf{T}}\cdot\boldsymbol{\tau}\cdot\nabla\mathbf{N^T})\mathbf{u}_e \\ &= \frac{1}{4\Delta^2}\mathbf{u}_e{}^{\mathbf{T}}(\mathbf{E^T}\boldsymbol{\tau}\mathbf{E})\mathbf{u}_e \end{aligned} \tag{9}$$

where $\mathbf{K}_{1e} = \frac{1}{4\Delta}\mathbf{E^T}\boldsymbol{\tau}\mathbf{E}$, and Δ denotes the area of this triangle, the subscript e represents the triangle element itself. Integral 1 can be written as Equation (10):

$$\begin{aligned} \int_e \frac{1}{2}[\nabla U\cdot(\boldsymbol{\tau}\nabla U)]d\Omega &= \frac{1}{2}\cdot\frac{1}{4\Delta^2}\int_e \mathbf{u}_e{}^{\mathbf{T}}\mathbf{E^T}\boldsymbol{\tau}\mathbf{E}\mathbf{u}_e d\Omega \\ &= \frac{1}{2}\mathbf{u}_e{}^{\mathbf{T}}\mathbf{K}_{1e}\mathbf{u}_e \end{aligned} \tag{10}$$

Similarly, integral 4 can be written as Equation (11):

$$\int_e [\nabla U\cdot(\boldsymbol{\tau}'\nabla U)]d\Omega = \mathbf{u}_e{}^{\mathbf{T}}\mathbf{K}'_{1e}\mathbf{u}_{0e} \tag{11}$$

where $\mathbf{K}'_{1e} = \frac{1}{4\Delta}\mathbf{E^T}\boldsymbol{\tau}'\mathbf{E}$.

Integrals 2 and 5 are $\int_e \left[\frac{1}{2}k^2\sigma_y U^2\right]d\Omega = \frac{1}{2}\mathbf{u}_e{}^T\mathbf{K}_{2e}\mathbf{u}_e$ and $\int_e [k^2\sigma'_y U^2]d\Omega = \mathbf{u}_e{}^T\mathbf{K}'_{2e}\mathbf{u}_{0e}$, where $\mathbf{K}_{2e} = \frac{\sigma_y k^2\Delta}{12}\begin{bmatrix}2&1&1\\1&2&1\\1&1&2\end{bmatrix}$ and $\mathbf{K}'_{2e} = \frac{\sigma'_y k^2\Delta}{12}\begin{bmatrix}2&1&1\\1&2&1\\1&1&2\end{bmatrix}$.

Integrals 3 and 6 are $\frac{1}{2}\int_e k\sigma_y\beta U^2 d\Gamma = \frac{1}{2}\mathbf{u}_e{}^T\mathbf{K}_{3e}\mathbf{u}_e$ and $\int_e k\sigma'_y\beta U U_0 d\Gamma = \mathbf{u}_e{}^T\mathbf{K}'_{3e}\mathbf{u}_{0e}$, where $\mathbf{K}_{3e} = \frac{l}{6}k\sigma_y\beta\begin{bmatrix}2&1\\1&2\end{bmatrix}$ and $\mathbf{K}'_{3e} = \frac{l}{6}k\sigma'_y\beta\begin{bmatrix}2&1\\1&2\end{bmatrix}$.

After assembling these elemental matrices, we obtain the system of linear equations (Xu 1994) for secondary potential shown in Equation (12):

$$\mathbf{KU} = -\mathbf{K'U}_0 \tag{12}$$

Simplification of the Euler angle

In Equations (8) and (12), to obtain the system of equations, we need the transformed primary potential U_0, i.e. the primary potential after Fourier transform. The analytical solution for the point source potential in an anisotropic 3-D half space is given by Li and Uren (1997a) and is shown in Equation (13).

$$u = \frac{I|\boldsymbol{\rho}|^{1/2}}{2\pi}\frac{1}{\sqrt{B}} \tag{13}$$

where $B = (\mathbf{r} - \mathbf{r_0})^T\cdot\boldsymbol{\rho}\cdot(\mathbf{r} - \mathbf{r_0})$. It is very difficult to apply the Fourier transform to Equation (13) after expanding B. As such, we assume that the medium near the point source (the background medium) is transverse isotropic, and the Euler angle is simplified as $\alpha = \beta = \gamma = 0^o$. The resistivity of the background medium is then written as Equation (14):

$$\rho = diag(\rho_x, \rho_y, \rho_z) \quad B = \frac{1}{\sqrt{\rho_y x^2 + \rho_y y^2 + \rho_z z^2}} \tag{14}$$

After applying the Fourier transform, the potential U_0 is written as Equation (15):

$$U_0(k, y, z) = \frac{I|\rho|^{1/2}}{2\pi}\sqrt{\sigma_y}K_0(k\sqrt{y^2 + \lambda z^2}) \tag{15}$$

We then bring Equation (15) into Equation (12) for each node, and obtain the linear equation; by solving that linear equation, we obtain the transformed secondary potential U. After inverse Fourier transform we get the secondary potential u shown in Equation (4), and the primary potential u_0 can be calculated from Equation (13), the total potential can then be achieved using Equation (4) (Xu, Duan, and Zhang 2000).

Algorithm validation

Figure 5 shows a two-layer vertical transverse isotropy model, which we used to test the accuracy of our algorithm.

The analytical solution (Xu 1994) and FE approach results with and without singularity removal are compared in Table 1. A unit current source (1A) is located at "A" in Figure 5, and the location of the electrode represents the distance between the electrode and the current source.

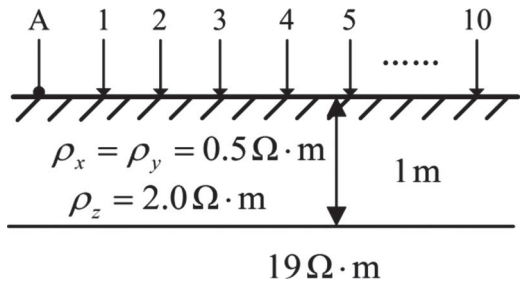

Figure 5. Two-layered earth with anisotropic covering.

Table 1. Compared analytical solutions for the finite element (FE) approach and the FE approach with singularity removal.

Electrode location x (m)	Analytical solutions (V)	FE approach (V)	Relative error (%)	FE with singularity removal (V)	Relative error (%)
1	0.3399	0.3510	3.2737	0.3378	0.6120
2	0.2538	0.2600	2.4406	0.2536	0.0827
3	0.2189	0.2204	0.7066	0.2193	0.2010
4	0.1968	0.1977	0.4289	0.1973	0.2388
5	0.1805	0.1802	0.2028	0.1810	0.2603
6	0.1676	0.1668	0.4738	0.1681	0.3043
7	0.1569	0.1560	0.5653	0.1573	0.2549
8	0.1478	0.1469	0.5956	0.1483	0.3179
9	0.1400	0.1391	0.6227	0.1405	0.3643
10	0.1331	0.1322	0.6636	0.1335	0.2930

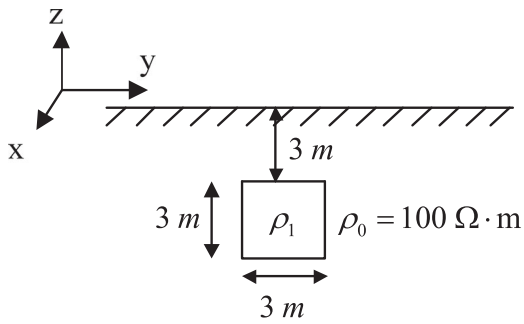

Figure 6. 2-D model with an anomalous body.

From Table 1, it is clear that FE with singularity removal achieved a very good accuracy and the relative error to the analytical solution is $<$ 1%, whereas that of the overall error of FE approach is larger than FE without singularity removal, especially near the point source, reaching 3.2%.

Influence of longitudinal and transverse resistivity on apparent resistivity

Forward modelling and analysis

To compare the effects of variations in longitudinal resistivity (ρ_L) and transverse resistivity (ρ_T) on apparent resistivity, we tested our algorithm on a simple model in which we vary both ρ_L and ρ_T. The anomalous body (Figure 6) is a square with a side length of 3 m buried at a depth of 3 m, and a background resistivity of $\rho_0 =$ 100 $\Omega\cdot$m. Three different resistivities are assigned to the anomalous body, and thus three models are tested.

Model 1: the anomalous body is isotropic, and $\rho_1 =$ 10 $\Omega\cdot$m; this model is abbreviated as MOD1.

Model 2: the anomalous body is anisotropic, the longitudinal resistivity is 10 $\Omega\cdot$m, and the transverse resistivity is the same as the background resistivity. $\rho_L =$ 10 $\Omega\cdot$m and $\rho_T =$ 100 $\Omega\cdot$m; this model is abbreviated as MOD2.

Model 3: the anomalous body is anisotropic, the transverse resistivity is 10 $\Omega\cdot$m, and the longitudinal resistivity is the same as the background resistivity. $\rho_L =$ 100 $\Omega\cdot$m and $\rho_T =$ 10 $\Omega\cdot$m; this model is abbreviated as MOD3.

There are 41 electrodes spaced uniformly (every 1 m) in the *y*-direction.

First, we test our algorithm on Wenner array data; testing all three models using four different AB spacings, 3, 7, 11 and 21 m. The results are summarised in Figure 7.

From Figure 7 it is apparent that the impact for the conductor is fairly small for a small AB spacing (3 m) because these short ABs sample only shallow subsurface information. When AB is large, the impact of the conductor shows in the apparent resistivity curves.

Additionally, we noticed from Figure 7 that the apparent resistivities of MOD3 change little when the AB spacing changes and the apparent resistivities are close to 100 $\Omega\cdot$m, which is the background resistivity. For MOD1 and MOD2, the apparent resistivity with a large AB (7, 11 and 21 m) shows low resistivities around the location of the anomalous body, and the curves of two models are similar for different AB distances. It can be concluded from the comparison that the Wenner array is sensitive to the longitudinal resistivity anomaly and is insensitive to the transverse resistivity anomaly.

Next, we tested our algorithm using other arrays: the pole–pole array and dipole–dipole array are simulated for three models, and the apparent resistivity pseudo-sections are shown in Figures 8 and 9, respectively.

The simulation results of the pole–pole array are similar to those of the Wenner array, where the transverse resistivity of the anomalous body has less influence on the simulation results and the anomalous amplitude caused by the anomalous body in the pole–pole array is less than that of the Wenner array. From Figure 8, we can see that the results of MOD1 and MOD2 are similar; the minimum apparent resistivity of MOD1 is 80 $\Omega\cdot$m and that of MOD2 is 90 $\Omega\cdot$m. However, it is found from the simulation results that when ρ_T is not consistent with background resistivity within the anomalous body, the apparent resistivity pseudo-section by the pole–pole array can reflect the location of the anomalous body more accurately in the *y*-direction.

From Figure 9, it is clear that the dipole–dipole array is better than the pole–pole array and Wenner array in detecting variation in the transverse resistivity because it shows a relatively large amplitude in the

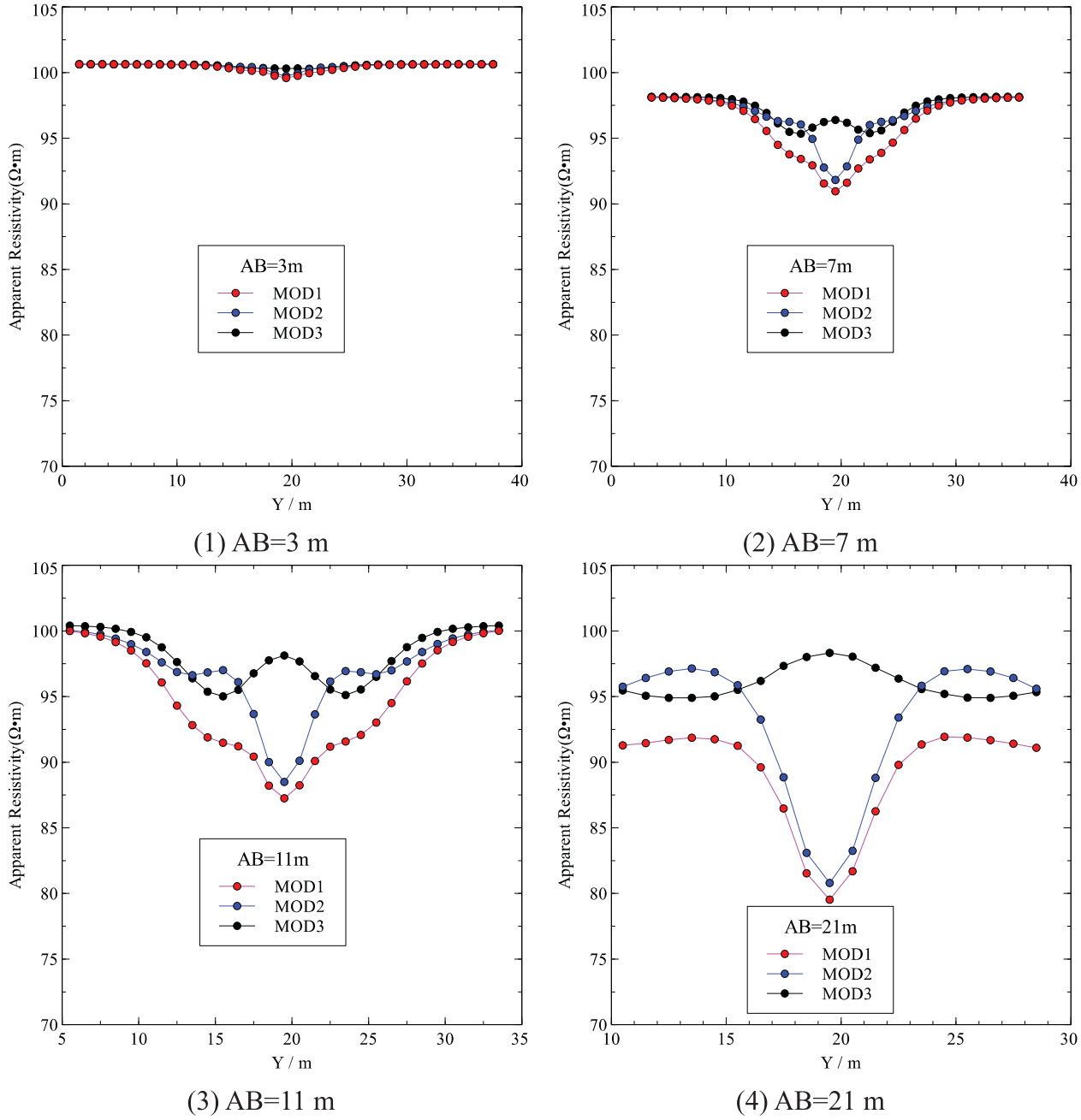

Figure 7. Apparent curves for three models for AB spacings: Wenner array.

apparent resistivity to transverse resistivity (Figure 9, 3). In addition, the transverse resistivity of the anomalous body also has a large influence on the apparent resistivity and is similar to the results of the isotropic model.

From the above simulation, we found that the longitudinal resistivity of the test cube has more influence on the measured apparent resistivities than the transverse resistivity. It is interesting that the sensitivity of each of the tested arrays to variation in longitudinal and transverse resistivity is different. Varying transverse resistivity has almost no effect on the apparent resistivity with the Wenner array, whereas the pole–pole array and dipole–dipole array can partially detect the transverse resistivity anomaly and even the position of the transverse resistivity anomaly.

Current density analysis

The origin of the three types of arrays that have different sensitivity to longitudinal and transverse apparent resistivity may influence ρ_L and ρ_T when current density is different. This leads to different potentials measured in the surface, and the apparent resistivities are then different. In the following sections, we test this using current flow simulation and analysis.

In this section, we analysed the different sensitivities to the longitudinal resistivity and transverse resistivity

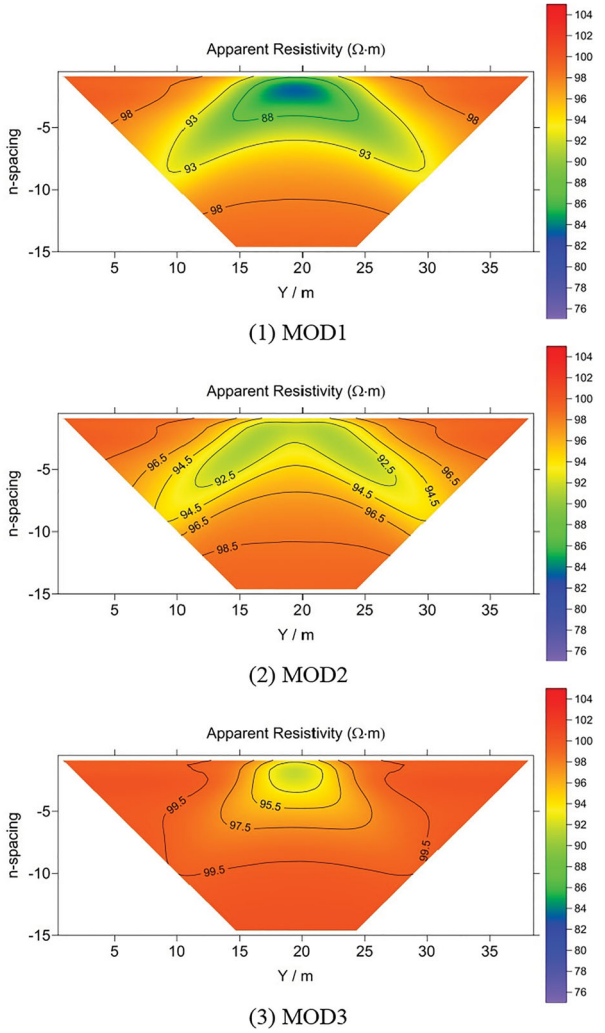

Figure 8. Apparent resistivity pseudo-sections for three models using the pole–pole array.

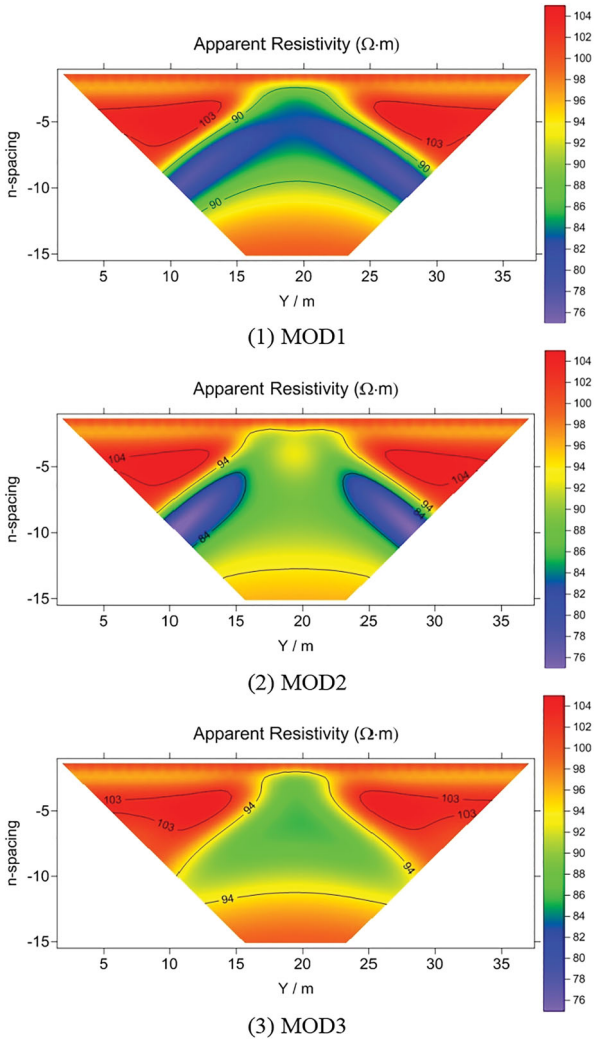

Figure 9. Apparent resistivity pseudo-sections for three models using the dipole–dipole array.

of the pole–pole array, Wenner array and dipole–dipole array from the perspective of current density.

The calculation of current density

Ohm's law can be expressed as Equation (16).

$$\mathbf{j} = \boldsymbol{\sigma}\mathbf{E} \tag{16}$$

In which,

$$\mathbf{j} = (j_x, j_y, y_z)^T \tag{17}$$

$$\mathbf{E} = (E_x, E_y, E_z)^T \tag{18}$$

For isotropic media, the conductor $\boldsymbol{\sigma} = \sigma$ is a scalar, so current density **j** and the electric field **E** are always parallel, whereas the earth is anisotropic, which means $\boldsymbol{\sigma} = \boldsymbol{\rho}^{-1}$ is a matrix and current density and electric field are in general no longer parallel (Li and Spitzer 2005). For the 2-D case, we choose the *y*–*z* plane as the research plane, the *x*-direction is the construction direction; the simplified conductor tensor is shown in Equation (19):

$$\boldsymbol{\sigma} = \begin{pmatrix} \sigma_{xx} & 0 & 0 \\ 0 & \sigma_{yy} & \sigma_{yz} \\ 0 & \sigma_{yz} & \sigma_{zz} \end{pmatrix} \tag{19}$$

Bring Equations (17), (18) and (19) to Equation (16), we can get the expression of current density in the *y*- and *z*-directions and written as Equation (20):

$$\begin{aligned} j_y(y,z) &= \sigma_{yy}E_y + \sigma_{yz}E_z \\ j_z(y,z) &= \sigma_{yz}E_y + \sigma_{zz}E_z \end{aligned} \tag{20}$$

The relationship between stationary electric field **E** and electric potential v is shown in Equation (21):

$$\mathbf{E} = -\nabla v \tag{21}$$

In the *y*–*z* plane, we have Equation (22).

$$\begin{aligned} E_y &= -\frac{\partial v}{\partial y} \\ E_z &= -\frac{\partial v}{\partial z} \end{aligned} \tag{22}$$

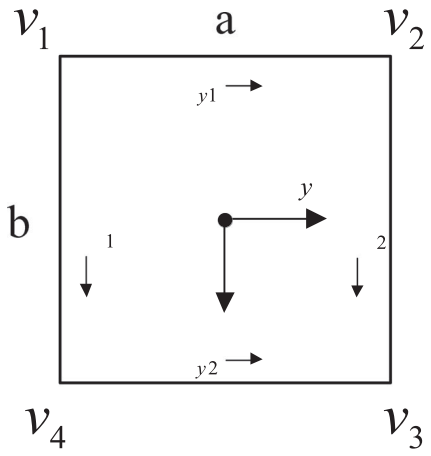

Figure 10. Use four rectangular nodes to calculate the electric field.

In which $\frac{\partial v}{\partial y}$ and $\frac{\partial v}{\partial z}$ are the derivatives of the space potential in *y*- and *z*-directions. Figure 10 shows a rectangle which is an element in the main computation area (Figure 2).

The electric field in the centre of the rectangle can be calculated with Equation (23).

$$E_y = \frac{E_{y1} + E_{y2}}{2}$$
$$E_z = \frac{E_{z1} + E_{z2}}{2} \tag{23}$$

The partial derivatives shown in Equation (22) can be calculated using Equation (24) within the rectangle.

$$E_{y1} = -\frac{\partial v}{\partial y}_1 = -\frac{v_2 - v_1}{2a}, E_{y2} = -\frac{\partial v}{\partial y}_2 = -\frac{v_3 - v_4}{2a}$$
$$E_{z1} = -\frac{\partial v}{\partial z}_1 = -\frac{v_4 - v_1}{2b}, E_{z2} = -\frac{\partial v}{\partial z}_2 = -\frac{v_3 - v_2}{2b} \tag{24}$$

Finally, we have Equation (25).

$$E_y = -\frac{v_2 - v_1 + v_3 - v_4}{2a}$$
$$E_z = -\frac{v_4 - v_1 + v_3 - v_2}{2b} \tag{25}$$

In which v_1, v_2, v_3, v_4 is the potential at the corner of the element, and is also the solution of our FEM. We can then get current density from Equations (20) and (25).

Current point source

Based on the results of the previous section, Figure 11 shows the current density and direction for a homogeneous half-space ($\rho_0 = 100\ \Omega \cdot$ m). In this example, 41 electrodes were deployed on the surface with uniform spacing of 1 m. A unit current source (1 A, used for all the examples shown here) was placed at the fifth electrode.

The arrows in the figure represent the direction of the current. To highlight the range of the current density, the logarithm to the base 10 is taken as the amplitude of the current density in the figure. Label "A" in the figure represents the current point source.

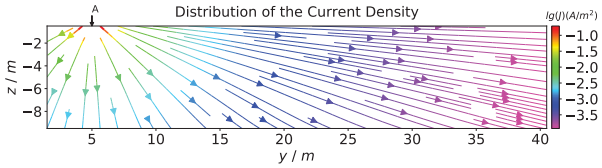

Figure 11. Uniform half-space current density distribution caused by a current point source.

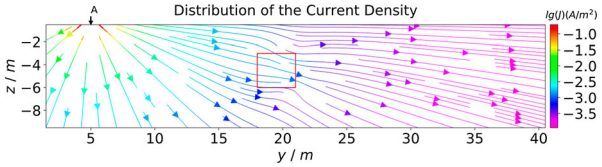

Figure 12. Current density distribution for MOD1 caused by a current point source.

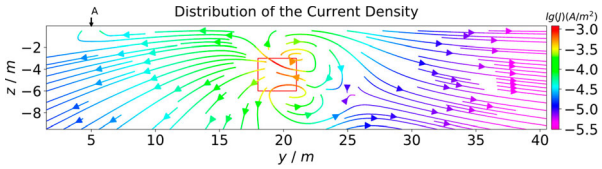

Figure 13. Difference between the half-space current density and MOD1 current density, using current point source.

It is apparent in Figure 11 that the current flows mainly along horizontal paths at a certain distance from point A in the *y*-direction, and the amplitude of the current density drops by r^3 after a certain distance from source point.

For MOD1, the current density distribution underground is shown in Figure 12 (the location of the 3 × 3 m test cube is highlighted in red in Figure 12).

It is clear in Figure 12 that the current density around the red rectangle is affected by the low-resistivity anomalous body, and the current converges to the rectangle on the side near the current source A. Obviously, this agrees with Ohm's law.

If the current density in Figure 11 (half-space current density distribution) is subtracted from the current density in Figure 12, the difference between the two is obtained as shown in Figure 13.

It is clear in Figure 13 that the difference in the current density distribution between the two models is largest in the vicinity of the anomalous body (red rectangle), and the maximum anomalous amplitude is also located in the red rectangle.

For MOD2, the current flows mainly along the *y*-direction in the red rectangle frame in Figure 14 because within the rectangle $\rho_L = 10\ \Omega \cdot$ m (a relatively low resistivity) leads the current to flow horizontally. Similarly, for MOD3 (Figure 15), the transverse resistivity of

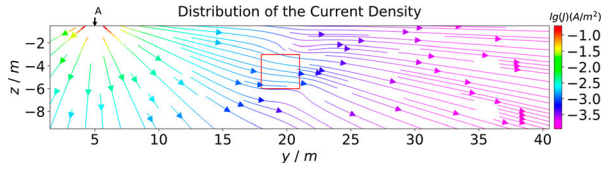

Figure 14. Current density distribution for MOD2 caused by a current point source.

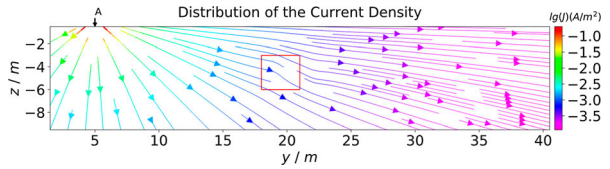

Figure 15. Current density distribution for MOD3 caused by a current point source.

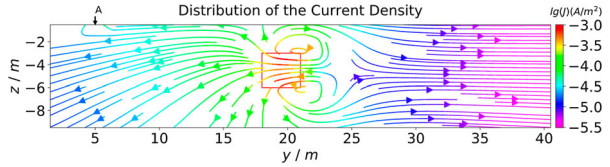

Figure 16. Difference between half-space current density and MOD2 current density, using current point source.

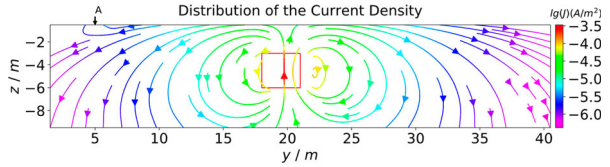

Figure 17. Difference between half-space current density and MOD3 current density, using current point source.

the anomalous body is relatively low ($\rho_T = 10\ \Omega \cdot \mathrm{m}$), so the current has a tendency to flow in the *z*-direction.

We subtracted the current density of MOD2 and MOD3, respectively, from the current density of half-space to produce two different current densities, shown in Figures 16 and 17.

From the distribution of the current density difference shown in Figures 16 and 17, it is clear that the variations in current density are concentrated mainly in the rectangle region where the anomalous body is located. The resistivity distribution difference between the half-space and MOD2 is the longitudinal resistivity within the rectangle region, which results in an anomalous current that flows mainly in the *y*-direction. The difference between the half-space and MOD3 shows a similar result. Both ρ_L and ρ_T could induce the current abnormity with a point source, and therefore, we can measure the apparent resistivity anomaly. Because the anomalous amplitude shown in Figure 17 is relatively weak compared with that in Figure 16, the measured anomalous apparent resistivity is lower.

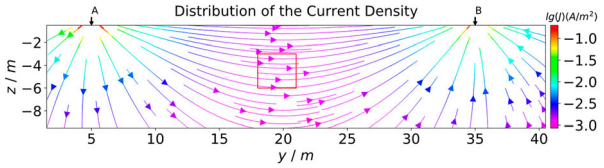

Figure 18. Current distribution of half-space caused by the Wenner array.

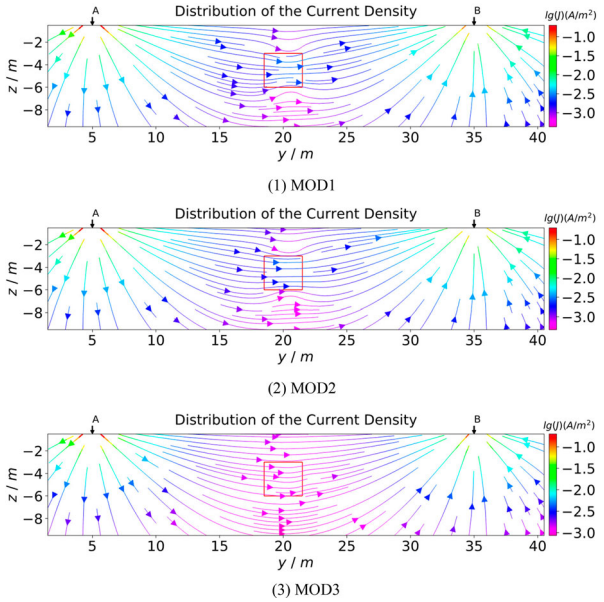

Figure 19. Current distribution of three models using the Wenner array.

Wenner array

When we supply a 1 A current into the ground at electrode 5, and a −1 A current at electrode 35, the current density distribution of the half-space is that shown in Figure 18.

The measured domain is between the two sources for the Wenner array. It is apparent that the current flows mainly in the *y*-direction in Figure 18, so we could infer that the Wenner array has little ability to detect variation in the *z*-direction.

Similarly, we calculate the current densities of three models, as shown in Figure 19.

It is apparent in Figure 19 that the current distributions for MOD1 and MOD2 are similar, and the current distribution for MOD3 is similar to that of the half-space shown in Figure 18. Similarly, we subtracted the current densities of MOD1, MOD2 and MOD3 from the current density of the half-space to produce three different current densities as shown in Figure 20.

It is clear that the anomalous currents caused by MOD1 and MOD2 are similar and flow mainly in the *y*-direction, therefore the apparent resistivity pseudo-sections of MOD1 and MOD2 are similar. The anomalous current caused by MOD3 within the rectangle region is mainly in the *z*-direction, and the amplitude of the anomalous current is one order of magnitude smaller

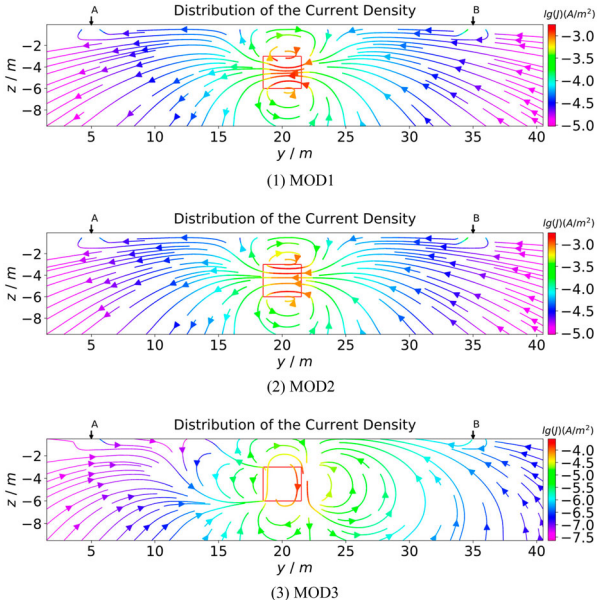

Figure 20. Difference between half-space mode current density and three different models of current density using the Wenner array.

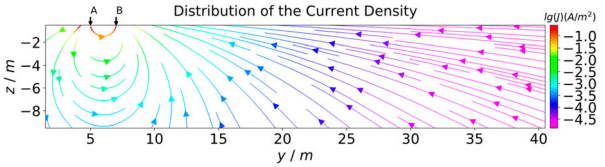

Figure 21. Current distribution of half-space caused by the dipole source.

than that of MOD1 and MOD2, so we barely observed the response in the apparent resistivity for MOD3 using the Wenner array.

From the simulation above, we can see that the Wenner array is not sensitive to transverse resistivity because its current density flows mainly in the *y*-direction, and the apparent resistivity anomalies are caused mainly by longitudinal resistivity.

Dipole–dipole array

For a dipole source, electrodes 5 and 7 are supplied with currents of 1 A and −1 A, respectively, and the current density distribution for the half-space is shown in Figure 21.

The current flows mainly in the *y*-direction directly below the dipole source (electrodes 5–7) and in the *z*-direction around electrodes 10–15. This finding explains the ability of the dipole–dipole array to explore longitudinal resistivity.

Similarly, the current density distribution for three models are shown in Figure 22.

From Figure 22, we can see that the current distribution is distorted in the vicinity of the anomalous body, and the anomalous current distributions are shown in Figure 23.

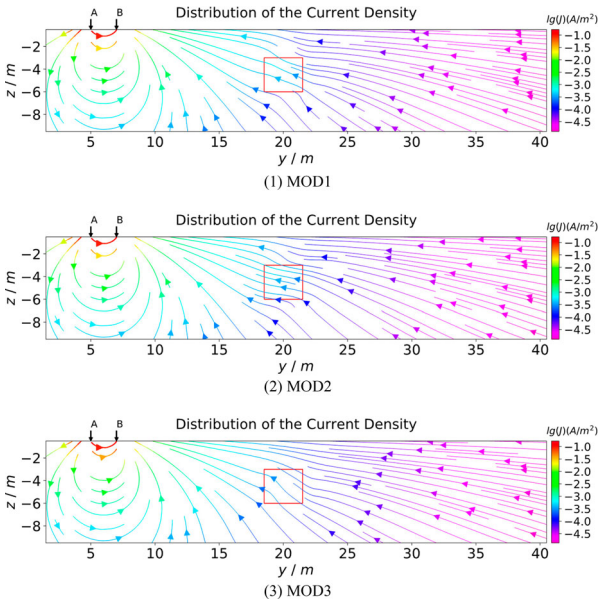

Figure 22. Current distribution of three models by dipole source.

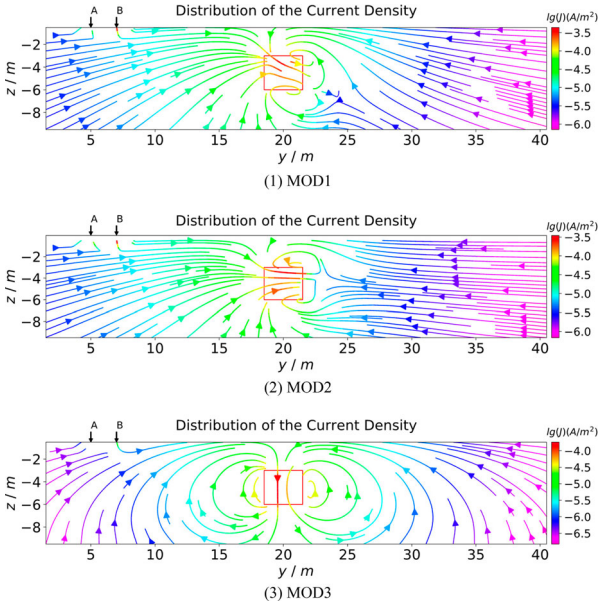

Figure 23. Difference between half-space mode current density and three different models of current density using the dipole source.

The anomalous current caused by MOD2 flows mainly in the *y*-direction, and the one caused by MOD3 flows mainly in the *z*-direction, whereas the one caused by MOD1 is flows in the *y*–*z*-direction. It is similar to the pole source, the amplitude of anomalous current for MOD3 is relatively weak compared with that of MOD1 and MOD2, so the measured anomalous apparent resistivity is lower.

For MOD2, when the dipole source moves above the anomalous body, the ρ_L of the body affects the current flow, mainly in the *y*-direction, so we can measure the anomalous potential on the surface of the ground. The measuring point is located in the blue region shown in

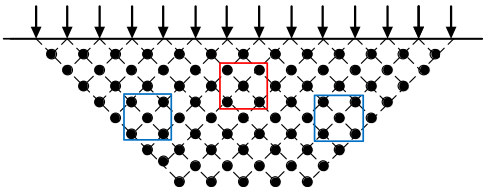

Figure 24. Dipole–dipole array.

Figure 24 in this situation, which is away from the location of the anomalous body. When the dipole source is away from the anomalous body (for example, near electrodes 15–17), the current flows mainly in the *z*-direction, where ρ_T is equal to the background resistivity. As such, the current is less affected. Therefore, the measured apparent resistivity is less affected too, and the measured point is located in the red rectangle in Figure 24. From the analysis above, we explained the apparent resistivity pseudo-section in Figure 9 (2) from the perspective of current flow.

Similarly, for MOD3, it is apparent that the apparent resistivity in the red region of Figure 24 is affected by anomalous resistivity (ρ_T), whereas the apparent resistivity in the blue region is close to the background resistivity (ρ_L).

Conclusions

In this paper, we present an FE algorithm for 2.5-D DC resistivity modelling in anisotropic media with singularity removal and present a simple analytical example that verifies the accuracy of our algorithm. Through simulation of the response using the pole–pole, dipole–dipole and Wenner arrays, we found that each array has a different sensitivity to variations in transverse and longitudinal resistivity, and the following conclusions were made:

(1) In general, for each array of the DC resistivity sounding, the influence of the longitudinal resistivity is greater than that of the transverse resistivity.
(2) The Wenner array is not sensitive to variation in the transverse resistivity.
(3) The pole–pole array is better than the Wenner array for detecting transverse resistivity anomalies.
(4) The amplitude of the apparent resistivity by the pole–pole array to anomalies is relatively small, but it always reflects the position of the anomalous body, either with longitudinal anomalies or transverse anomalies.
(5) The dipole–dipole array produces a larger apparent resistivity of anomalies in both the longitudinal and transverse resistivity anomalies. Longitudinal resistivity anomalies appear on both sides of the anomalous body, and transverse anomalies appear in the vicinity of the anomalous body.

By calculating the current density, we analysed the different exploration capabilities of each array for longitudinal and transverse resistivity from the perspective of current density, with the distribution characteristics of the current density underground. When the distance between two point sources of the Wenner array is large, the current in the target area flows mainly in the *y*-direction, so it has good resolution with regard to the longitudinal resistivity anomaly. However, dipole–dipole sources have different distribution characteristics of current flow in the subsurface variety from the position, so the dipole–dipole array has improved ability to detect variation in both longitudinal and transverse resistivity anomalies.

In the field, if we "know" the electrical anisotropy of the target geological body in the study area, we can adopt suitable arrays through forward modelling to improve exploration results.

Funding

This work was supported by the National Key R&D Program of China (2016YFC0600505) and the National Natural Science Foundation of China (41425017). We want to thank to four anonymous reviewers for critical reviews and comments.

ORCID

Tao Song http://orcid.org/0000-0002-6431-6325

References

Asten, M. W. 1974. The influence of electrical anisotropy on mise à la masse surveys. *Geophysical Prospecting* 22: 238–45.

Dey, A., and H. F. Morrison. 1979. Resistivity modelling for arbitrarily shaped two-dimensional structures*. *Geophysical Prospecting* 27: 106–36.

Greenhalgh, S., T. Wiese, and L. Marescot. 2010. Comparison of DC sensitivity patterns for anisotropic and isotropic media. *Journal of Applied Geophysics* 70: 103–12.

Li, Y., and K. Spitzer. 2002. Three-dimensional DC resistivity forward modelling using finite elements in comparison with finite-difference solutions. *Geophysical Journal International* 151: 924–34.

Li, Y., and K. Spitzer. 2005. Finite element resistivity modelling for three-dimensional structures with arbitrary anisotropy. *Physics of the Earth and Planetary Interiors* 150: 15–27.

Li, P., and N. F. Uren. 1997a. Analytical solution for the point source potential in an anisotropic 3-D half-space I: Two-horizontal-layer case. *Mathematical and Computer Modelling* 26: 9–27.

Li, P., and N. F. Uren. 1997b. Analytical solution for the point source potential in an anisotropic 3-D half-space II: With two-vertical boundary planes. *Mathematical and Computer Modelling* 26: 29–52.

Li, P., and N. F. Uren. 1997c. The modelling of direct current electric potential in an arbitrarily anisotropic half-space containing a conductive 3-D body. *Journal of Applied Geophysics* 38: 57–76.

Lindell, I. V., M. E. Ermutlu, K. I. Nikoskinen, and E. H. Eloranta. 1993. Static image principle for anisotropic-conducting

half-space problems: PEC and PMC boundaries. *Geophysics* 58: 1861–4.

Lowry, T., M. B. Allen, and P. N. Shive. 1989. Singularity removal: A refinement of resistivity modeling techniques. *Geophysics* 54: 766–74.

Penz, S., H. Chauris, D. Donno, and C. Mehl. 2013. Resistivity modelling with topography. *Geophysical Journal International* 194: 1486–97.

Ren, Z., and J. Tang. 2010. 3D direct current resistivity modeling with unstructured mesh by adaptive finite-element method. *Geophysics* 75: H7–H17.

Ren, Z., and J. Tang. 2014. A goal-oriented adaptive finite-element approach for multi-electrode resistivity system. *Geophysical Journal International* 199: 136–45.

Wang, W., X. Wu, and K. Spitzer. 2013. Three-dimensional DC anisotropic resistivity modelling using finite elements on unstructured grids. *Geophysical Journal International* 193: 734–46.

Wiese, T., S. Greenhalgh, B. Zhou, M. Greenhalgh, and L. Marescot. 2015. Resistivity inversion in 2-D anisotropic media: numerical experiments. *Geophysical Journal International* 201: 247–66.

Wu, X., Y. Xiao, C. Qi, and T. Wang. 2003. Computations of secondary potential for 3D DC resistivity modelling using an incomplete Choleski conjugate-gradient method. *Geophysical Prospecting* 51: 567–77.

Xu, S. 1994. *Finite element method in geophysics*. Beijing: Science Press [in Chinese].

Xu, S., B. Duan, and D. Zhang. 2000. Selection of the wavenumbers k using an optimization method for the inverse Fourier transform in 2.5D electrical modelling. *Geophysical Prospecting* 48: 789–96.

Yin, C. 2000. Geoelectrical inversion for a one-dimensional anisotropic model and inherent non-uniqueness. *Geophysical Journal International* 140: 11–23.

Yin, C., and P. Weidelt. 1999. Geoelectrical fields in a layered earth with arbitrary anisotropy. *Geophysics* 64: 426–34.

Zhao, S., and M. J. Yedlin. 1996. Some refinements on the finite-difference method for 3-D dc resistivity modeling. *Geophysics* 61: 1301–7.

Zhou, B., M. Greenhalgh, and S. A. Greenhalgh. 2009. 2.5-D/3-D resistivity modelling in anisotropic media using Gaussian quadrature grids. *Geophysical Journal International* 176: 63–80.